RESEARCH ARTICLE

Interconnection between the Indian and the East Asian summer monsoon: Spatial synchronization patterns of extreme rainfall events

Shraddha Gupta[1,2] | Zhen Su[1,3] | Niklas Boers[1,4,5] | Jürgen Kurths[1,2] | Norbert Marwan[1,6] | Florian Pappenberger[7]

[1]Potsdam Institute for Climate Impact Research (PIK)–Member of the Leibniz Association, Potsdam, Germany

[2]Department of Physics, Humboldt University at Berlin, Berlin, Germany

[3]Department of Computer Science, Humboldt University at Berlin, Berlin, Germany

[4]Department of Earth System Modelling, School of Engineering & Design, Technical University of Munich, Munich, Germany

[5]Global Systems Institute and Department of Mathematics, University of Exeter, Exeter, UK

[6]Institute for Geosciences, University of Potsdam, Potsdam, Germany

[7]European Centre for Medium-Range Weather Forecasts, Reading, UK

Correspondence
Shraddha Gupta and Zhen Su, Potsdam Institute for Climate Impact Research (PIK), Telegrafenberg A56, Potsdam 14473, Germany.
Email: shraddha.gupta@pik-potsdam.de (S.G.) and
Email: zhen.su@pik-potsdam.de (Z.S.)

Abstract

A deeper understanding of the intricate relationship between the two components of the Asian summer monsoon (ASM)—the Indian summer monsoon (ISM) and the East Asian summer monsoon (EASM)—is crucial to improve the subseasonal forecasting of extreme precipitation events. Using an innovative complex network-based approach, we identify two dominant synchronization pathways between ISM and EASM—a southern mode between the Arabian Sea and southeastern China occurring in June, and a northern mode between the core ISM zone and northern China which peaks in July—and their associated large-scale atmospheric circulation patterns. Furthermore, we discover that certain phases of the Madden–Julian oscillation and the lower frequency mode of the boreal summer intraseasonal oscillation (BSISO) seem to favour the overall synchronization of extreme rainfall events between ISM and EASM while the higher-frequency mode of the BSISO is likely to support the shifting between the modes of ISM–EASM connection.

KEYWORDS
complex networks, East Asian summer monsoon, event synchronization, extreme precipitation, Indian summer monsoon, Intraseasonal oscillation

1 | INTRODUCTION

The Asian summer monsoon (ASM) is an important component of the global climate system. It is a planetary-scale phenomenon involving the annual migration of the Intertropical Convergence Zone. The ASM is characterized by a distinct seasonal reversal of low-level wind fields accompanied by heavy rainfall. It can be divided into two main subsystems, namely the Indian summer monsoon (ISM) and the East Asian summer monsoon (EASM). A large amount of literature has contributed to the study of both monsoon systems and their connections (Goswami and Mohan, 2001; Ding and Wang, 2005; Rajeevan et al., 2010; Ding et al., 2020). While both subsystems have profound differences, they strongly influence each other (Ding, 1994; Ding and Chan, 2005; Feldhoff et al., 2012; Rehfeld et al., 2013). The ASM has a huge socioeconomic impact in South and East Asia; therefore, the understanding of its underlying complex interconnectivity structure is crucial.

The ISM is known to have significant impact on rainfall over northern China (Kripalani and Singh, 1993; Kripalani and Kulkarni, 2001; Liu and Ding, 2008b; Wu, 2017; Beverley et al., 2021). Several studies also investigated the relationship between ISM onset and the onset of the Meiyu season over the Yangtze River Valley in China (Liu and Ding, 2008a; Liu et al., 2019). Some authors have referred to the above relationships between rainfall over India and that over East Asia as the two modes of ISM–EASM teleconnection (Liu and Ding, 2008a, 2008b; Liu et al., 2019; Woo et al., 2019). Most of these studies primarily rely on methods of correlation, empirical orthogonal functions (EOFs) and composite analyses. However, these methods are often not sufficient for analysing the spatial characteristics of extreme rainfall covariability. Furthermore, analyses based on correlations alone typically do not allow identifying the specific times associated with a particular climate interaction pattern.

Here, we address the above problems using a method based on the combination of a nonlinear synchronization measure and complex network theory. Recently, complex networks have been applied to study both the regional and global patterns of extreme rainfall (Malik et al., 2012; Boers et al., 2013; 2014; Stolbova et al., 2014; Boers et al., 2019). They have been used, in particular, to reveal spatiotemporal patterns of synchronous heavy rainfall associated with both the ISM (Malik et al., 2012; Stolbova et al., 2014; Di Capua et al., 2020) and the EASM (Marwan and Kurths, 2015; Runge et al., 2015; Wolf et al., 2021) separately. We go a step further here, by investigating the interaction between these two subsystems of the ASM. By constructing climate networks using

extreme precipitation spatiotemporal data for the monsoon season, extracted from the satellite-derived and gauge-calibrated TRMM 3B42V7 (Huffman et al., 2007) rainfall dataset, we show that the connection between ISM and EASM has two different modes which are separated both spatially and temporally. Moreover, we provide a comprehensive picture of the large-scale atmospheric circulation patterns associated with each mode of connection.

The various modes of the tropical intraseasonal oscillations (ISO) (Goswami and Mohan, 2001; Serra et al., 2014)—the eastward propagating Madden–Julian oscillations (MJO) (Madden and Julian, 1994; Wheeler and Hendon, 2004) and the northward propagating boreal summer intraseasonal oscillation (BSISO) (Yasunari, 1979; Murakami, 1983; Wang et al., 2005; Yun et al., 2008; Lee et al., 2013a)—are known to have considerable influence on the variability of the global monsoon system at intraseasonal timescales. Numerous studies have investigated the impact of the ISO on the different aspects of the ISM and the EASM, individually. However, not much attention has been given to the possible influence of the ISO on the intraseasonal variability of the ISM–EASM connection. Therefore, as a final step, we investigate the potential role of the different modes of the ISO by studying the distribution of the MJO/BSISO phases of those days when there is high synchronization of extreme rainfall events between the ISM and the EASM.

2 | METHODS

2.1 | Data

We analyse the satellite-derived Tropical Rainfall Measurement Mission (TRMM 3B42 V7; Huffman et al., 2007) total precipitation data, with daily temporal resolution, provided on a spatial grid with resolution of $0.25° \times 0.25°$, ranging from 50°N to 50°S, for the time period 1998–2019 (https://disc.gsfc.nasa.gov/, last accessed: 8th September 2020). The spatial domain of this study is confined to the region 0° to 50°N and 60°E to 160°E for the functional network analysis, which gives 80,000 grid points. It is worth mentioning here that although satellite rainfall products are known to underestimate extreme precipitation (Libertino et al., 2016), their high spatiotemporal resolution and almost global coverage make them convenient to study spatial patterns of precipitation.

Data for atmospheric variables, such as wind components and geopotential height (GPH) at pressure levels of 250, 500 and 850 hPa, vertically integrated water vapour

flux and outgoing long-wave radiation (OLR), are obtained from the ERA5 reanalysis (Hersbach *et al.*, 2020) at daily temporal and $1° \times 1°$ spatial resolutions for the same time period (https://cds.climate.copernicus.eu/, last accessed: 9th December 2020). Analysis of their composite anomalies is done over an extended spatial region (15°S to 50°N and 0° to 160°E).

The Real-Time Multivariate MJO indices (RMM1 and RMM2) of (Wheeler and Hendon, 2004)—based on a pair of empirical orthogonal functions (EOFs) of the combined fields of near-equatorially averaged 850-hPa zonal wind, 200-hPa zonal wind and OLR data—were used for defining the various Phases of the MJO (http://www.bom.gov.au/climate/mjo/, last accessed: 22nd November 2021). The phases of the BSISO were defined using the real-time indices BSISO1 and BSISO2 proposed by Lee *et al.* (2013a), which are based on a multivariate EOF analysis of daily anomalies of OLR and zonal wind at 850 hPa (U850) in the region 10°S–40°N, 40°–160°E (https://apcc21.org/ser/moni.do/, last accessed: 22nd November 2021).

2.2 | Extreme rainfall events

Extreme rainfall events (EREs) are identified as days with total rainfall sums greater than the 90th percentile of wet days (rainfall >1 mm) at each grid point, for the particular month (June, July or August) or the season under consideration (here, the monsoon season from June to August, JJA). The events are de-clustered by counting consecutive days with rainfall above the threshold as a single event placed on the first day of occurrence.

2.3 | Functional network analysis

2.3.1 | Event synchronization

We employ here event synchronization (ES) (Quiroga *et al.*, 2002) as an event-based similarity measure to quantify synchronous EREs at different locations occurring at varying temporal delays. This synchronization measure has been successfully applied to analyse global and regional extreme rainfall patterns (Malik *et al.*, 2012; Boers *et al.*, 2013, 2014; Stolbova *et al.*, 2014; Boers *et al.*, 2019). Let us consider two event series $\left\{e_i^\mu\right\}_{\mu=1,..,l_i}$ and $\left\{e_j^\nu\right\}_{\nu=1,..,l_j}$ with l_i and l_j events, respectively, corresponding to grid points i and j, where e_i^μ denotes the time stamp of the μth event observed at grid point i. Two events e_i^μ and e_j^ν can be uniquely associated with each other if the absolute value of the temporal delay between them ($t_{i,j}^{\mu,\nu} := |e_i^\mu - e_j^\nu|$) is less than a *dynamical delay* defined by

$\tau_{i,j}^{\mu,\nu} := \frac{\min\left\{t_{i,i}^{\mu,\mu-1},\ t_{i,i}^{\mu,\mu+1},\ t_{j,j}^{\nu,\nu-1},\ t_{j,j}^{\nu,\nu+1}\right\}}{2}$. To confine the synchronization time scale, the maximum temporal delay allowed is $\tau_{\max} = 7$ days. ES_{ij} gives the number of such uniquely associable, that is, synchronous, pairs between the two event series. An advantage of ES over ordinary lead–lag correlation analyses is that it allows for a dynamical delay in the range $[0, \tau_{\max}]$ instead of a static choice of delay for the entire time series. Moreover, it takes into account a potentially changing density of events.

2.3.2 | Network construction

The nodes of our functional network are the spatial grid points of the TRMM precipitation data with their corresponding ERE series (see section 2.2). ES_{ij} is computed for all pairwise combinations of grid points, $i, j = 1, ..., N$, where $N = 80,000$ by the above procedure. The statistical significance of each empirical value ES_{ij} is determined on the basis of a null model distribution which is numerically obtained by computing ES for 2000 pairs of surrogate event series with l_i and l_j uniformly and randomly distributed events. Finally, a network link is placed between grids i and j if ES_{ij} is significant at a significance level of 0.05 (i.e., ES_{ij}>95th percentile of the corresponding null model distribution). The network adjacency matrix A_{ij} is then constructed by setting $A_{ij}=1$ if there is a link between nodes i and j, and $A_{ij}=0$ otherwise. The spatial patterns of network degree depend only weakly on the choice of the significance threshold, ranging from the 95th to the 99.5th percentile of the null model distribution. Our results are also robust to the choice of different maximum temporal delay between synchronous events, $\tau_{\max} \in [3, 15]$ days. All our results remain similar for the case when EREs are defined as events above the 95th instead of the 90th percentile (not shown).

We construct three separate networks using the above method for the successive months of June, July and August, using EREs calculated from the daily rainfall of the respective month (see section 2.2) to observe monthly evolution of the connectivity structure of the region during the monsoon season. A separate network is also constructed for the whole JJA season using EREs computed from the JJA daily rainfall.

2.3.3 | Network measures

After the network is constructed, we compute the node-base network measure *degree*. The degree k_i of a node i in a network is defined as the number of connections it has to all other nodes,

$$k_i = \sum_{j=1}^{n} A_{ij}. \tag{1}$$

In this case, the degree at a given grid point gives the number of those grid points where extreme rainfall occurs synchronously. Regions of higher degree are of particular importance for identifying large-scale synchronization of extreme rainfall and their causes (Malik *et al.*, 2012; Boers *et al.*, 2014; Stolbova *et al.*, 2014).

We also calculate the partial degree $\{k_i\}_R$ of the nodes in the network linked to a particular region R, which yields the number of links connecting a node i outside R with the nodes within R. This gives a selective view of the degree plot to identify regions in the network connected to a specific area. This approach leads to a visualization that reveals the various modes of connections among the different regions.

2.3.4 | Identification of days of high rainfall synchronicity

A modification of ES described in section 2.3.1 allows to determine the specific days when high event synchronization of extreme rainfall occurs between two regions of interest, while keeping track of the temporal order (Boers *et al.*, 2019). Consider two sets of time series, A and B corresponding to two different regions of interest. We compute $\mathrm{ES}_{A \to B}^{\mu}$ $(\mathrm{ES}_{B \to A}^{\nu})$ by counting the number of events in region A (B) that have a subsequent uniquely associable event in region B (A). Then, a Butterworth low-pass filter with a cutoff frequency of 7 days is applied to the time series of $\mathrm{ES}_{A \to B}^{\mu}$ $(\mathrm{ES}_{B \to A}^{\nu})$ so obtained. Finally, the days of high synchronization between the two regions are determined by identifying the local maxima of the time series that are above the 90th percentile of the entire time series. The specific time points so obtained are then used to compute the composite anomalies of rainfall (from TRMM) and other atmospheric variables (from ERA5).

2.4 | Lead–lag correlation analysis

We get two time series by spatially averaging the daily number of EREs in the two given regions of interest, and the high-frequency noise is then eliminated by passing them through a Butterworth low-pass filter with a cutoff period of 7 days. A lead–lag correlation analysis is then performed between both time series by computing the Spearman rank correlation between the first time series and the lagged values of the second time series, with lags varying in the range $[-30, 30]$ days. The results remain very similar when the cutoff period of the Butterworth filter is varied within a range of 7–11 days (not shown). This analysis helps us to obtain the duration by which one series leads or trails behind the other which gives us a preliminary idea about how long it may take for the effect to propagate from one region to the other and, hence, establish the connection. It serves as an additional step to see if the two connected regions obtained for the network are indeed significantly correlated. The information of the time lags at which high correlation occurs, is useful to compute the composites of vertically integrated water vapour flux in order to trace the path of the moisture transport between the interacting regions.

3 | RESULTS AND DISCUSSION

In this section, we first present our results based on the functional network analysis (see section 2.3). From the spatial patterns of degree of the extreme precipitation networks, we identify the regions associated with the ISM and the EASM that show the strongest connections. Thereafter, we investigate the mechanism underlying these synchronization pathways based on the associated atmospheric circulation features. Finally, we study the potential influence of ISO on variability of the ISM–EASM interconnection at intraseasonal timescales.

3.1 | Network analysis: Spatial degree patterns

The spatial pattern of degree (see section 2.3.3) yielded from the climate network analysis (see section 2.3.2) of the chosen bounded region for the successive months of June, July and August, and the entire JJA season are shown in Figure 1a–d, respectively. From the monthly evolution of the degree configuration of the extreme precipitation network (Figure 1a–c), it is evident that—while there occurs an overall change in degree over the ISM, EASM and Pacific Ocean regions—two specific regions of the ISM show a pronounced change over these months. First, the Arabian Sea region (ARB, Figure 1) and adjacent coastal region of India exhibit a discernible decrease in degree when going from June to July. In addition, the northern and central part of India, which is often referred to as the core monsoon zone (CMZ; Figure 1) (Gadgil and Joseph, 2003; Rajeevan *et al.*, 2010) of the ISM shows a significant increase in degree in July and August in comparison with June. Interestingly, although the spatial degree pattern for the entire JJA season (Figure 1d) is qualitatively rather similar to that of the monthly
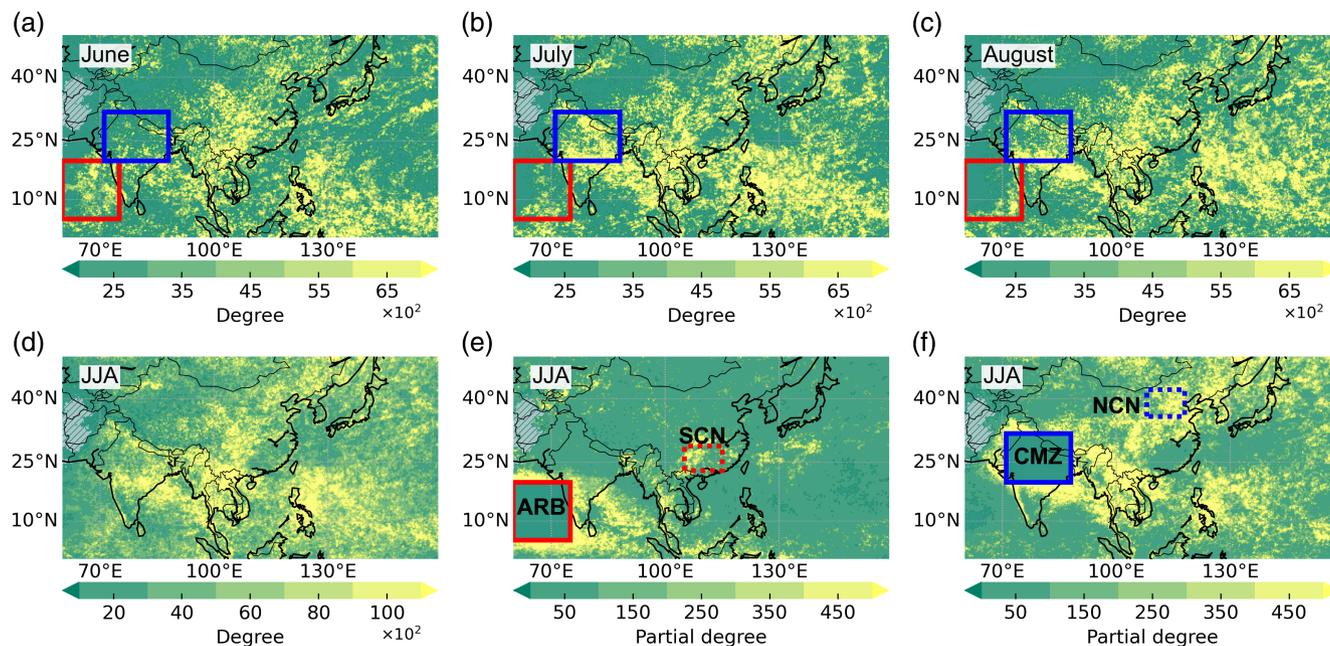
FIGURE 1 Monthly evolution of network degree for networks constructed for June (a), July (b) and August (c), respectively. The solid boxes are positioned at the Arabian Sea (ARB), and at the northern and central parts of India which is the core ISM zone (CMZ), respectively, to indicate noticeable changes in degree each month at different ISM regions. (d) Degree for the network constructed for the entire JJA season. (e, f) Partial degree for the regions, ARB (solid box: 5°–20°N, 60°–75°E) and CMZ (solid box: 20°–32°N, 71°–88°E), respectively, based on the network in (d) to indicate specific regions connected to each of them. From (e), it is seen that ARB has connections to southern China (SCN; dashed box: 23°–29°N, 105°–115°E) while from (f), CMZ is seen to be connected to parts in northern China (NCN; dashed box: 36°–42°N, 108°–118°E) [Colour figure can be viewed at wileyonlinelibrary.com]

networks (Figure 1a–c), we do not see a high-degree patch over ARB in the JJA network (Figure 1d), implying that links connecting ARB with other regions occur earlier but get overshadowed later in the season when the monsoon activity is at its peak and has moved inward into the subcontinent.

Therefore, we compute the partial degree (see section 2.3.3) corresponding to the JJA network in Figure 1d for the regions ARB and CMZ separately. This will help us to identify any changes in the spatial connectivity of these regions, which may occur over the course of the season. From the partial degree distribution of the region ARB shown in Figure 1e, we observe that apart from local connections with adjacent regions of the Indian peninsula and the Bay of Bengal, it has long-range connections to a region in southeastern China (SCN), roughly located in the middle and lower reaches of the Yangtze River basin, which receives persistent Meiyu rainfall (Ding and Chan, 2005; Ding et al., 2020). On the other hand, the CMZ region is well connected to the northern parts of China in the Yellow River basin (NCN) (Figure 1f). We hence identify two spatially and temporally separated ERE synchronization pathways between ISM and EASM regions: (a) ARB with SCN and (b) the CMZ with NCN. These two pairs form the southern (ARB-SCN) and the northern (CMZ-NCN) modes of the

ISM–EASM connection (Ding and Wang, 2005; Liu and Ding, 2008a; Liu and Ding, 2008b; Liu et al., 2019).

The distribution of the spatial distances across which significant synchronizations occur in case of the ASM regional network constructed for the JJA season exhibits a scale break at approximately 2,000 km (see Figure S1a, Supporting Information) similar to that shown by Boers et al. (2019) for a global extreme precipitation network indicating a physical regime shift. For distances (d) less than 2,000 km, the distribution shows a power-law decay ($p(d) \propto d^{-\alpha}$), with an exponent $\alpha = 0.83$, signifying links associated with regional weather systems. On the other hand, the distribution for longer distances (d > 2,000 km) follows closely the distribution of all possible great-circle distances on Earth's surface, implying that the links are potentially associated with global-scale teleconnections. It must be noted that the spatial patterns of the partial degree of ARB and CMZ computed by considering only links longer than 2,000 km (see Figure S1b,c) still show the significant connections to SCN and NCN, respectively, seen in Figure 1e,f, thereby implying that these two modes of connection between the ISM and the EASM are also part of the global-scale teleconnections.

Moreover, from the partial degree plots of Figure 1e,f, it should be noted that there are almost no links connecting ARB and SCN to NCN (Figures 1e and S2a), as well

as CMZ and NCN to SCN (Figures 1f and S2b). The asynchronicity of EREs between SCN and NCN (also seen from Figure S2a,b) along with significant change in degree of ARB and CMZ when evolving from June to July clearly indicate that the two connection modes occur at different times within the JJA season. The higher connectivity of nodes in ARB in June and its subsequent decrease in July, during times when connectivity is enhanced over CMZ, implies that the southern mode precedes the northern mode. The simultaneous occurrence of EREs in the regions ARB and SCN in June and that in the regions CMZ and NCN later in July and August can also be observed by defining an index for the northward movement of ISM and EASM based on the number of EREs, as described in Data S1 and Figure S3. In section 3.2, we show using event synchronization that the pairs of regions (ARB-SCN and CMZ-NCN) indeed have high synchronization of EREs at different times in the JJA season. We will in the following focus on understanding the mechanism of the two modes of the ISM–EASM connection. The solid and dashed boxes shown in Figure 1e,f are the representative regions chosen for ARB, SCN, CMZ and NCN for all further analysis.

CMZ also exhibits a very high number of links (Figure 1f) to regions of the western Pacific Ocean, the Philippine Sea and South China Sea, which also occur as patches of overall high degree in Figure 1d. The synchronous EREs in these regions are mostly due to typhoons, which are prevalent during the JJA season (Choi et al., 2010). We do not consider these regions in our further analysis, as we are more interested in monsoon-type rainfall than that from the thunderstorms. High total degree is also observed over northern Bay of Bengal, parts of northeast India, Tibetan Plateau and parts of Mainland Southeast Asia such as South Vietnam and Thailand (Figure 1d). These regions also experience rainfall from the southwesterly monsoon winds which explain their linkage with CMZ (Figure 1f).

Although extreme rainfall over southern Japan due to the Baiu front is also a part of the EASM system, it is less synchronous with ISM, as seen from Figure S2c (Kripalani and Kulkarni, 2001; Wu, 2017; Liu et al., 2019). However, there are links connecting southern Japan to SCN, as seen from Figure S2a,c, indicating the occurrence of synchronous frontal rainfall in both regions (Ding and Chan, 2005; Ding et al., 2020).

3.2 | Specific times of high extreme rainfall synchronicity

Next, we identify specific days during which extreme rainfall events occur synchronously in each of the two pairs of regions, viz., ARB-SCN and CMZ-NCN (see section 2.3.4). The month-wise distribution of the days of highest rainfall synchronicity is shown in Figure 2a. We see that the frequency of synchronous extreme rainfall occurrences for the southern mode of ISM–EASM connection is the highest in June and decreases sharply in July and August, while that for the northern mode peaks in July. This is consistent with our earlier observations in Figure 1. Moreover, the frequency of the high ERE synchronization times is seen to be higher at the beginning of June, which is the period of ISM onset. It also corroborates with previous studies of the interrelationship, which claimed that the southern mode is associated with the onset of the ISM in June and the Meiyu in Yangtze basin (Liu and Ding, 2008a). Ding and Wang (2005) speculated that the circumglobal teleconnection (CGT) plays an important role to connect ISM with rainfall over northern China and made an indirect inference about the time of the establishment of this relation being in late summer (July–August). Our results in Figure 2a directly confirm this conjecture.

### 3.2.1 | Lead–lag analysis of rainfall

Figure 2b,c shows a lead–lag analysis of the time series (see section 2.4), obtained by spatially averaging the numbers of EREs in each pair of regions, for the JJA season and for the month when the highest synchronization is observed for each mode, i.e., June for the southern mode and July for the northern mode. We find from Figure 2b that the correlation between ARB and SCN peaks at a lag of 4 days for the entire JJA season but is maximum at 14 days when only June is considered. However, interestingly, in case of the northern mode of ISM–EASM connection, we see from Figure 2c that the maximum correlation occurs at lag 0 during the JJA season and at a lag of 1–2 days for only July. The positive correlation between CMZ and NCN is in agreement with that observed by Kripalani and Kulkarni (2001) between summer monsoon rainfall over India and north China, indicating an in-phase relationship. Only those lags which have significantly high correlations ($p<.05$) were used to determine the local maximum peak. The rainfall composite anomalies (see Figure S4) also reflect the above findings.

3.3 | Atmospheric circulation composite anomalies

Next, we compute the composites of the anomalies of geopotential height, meridional wind speeds, and
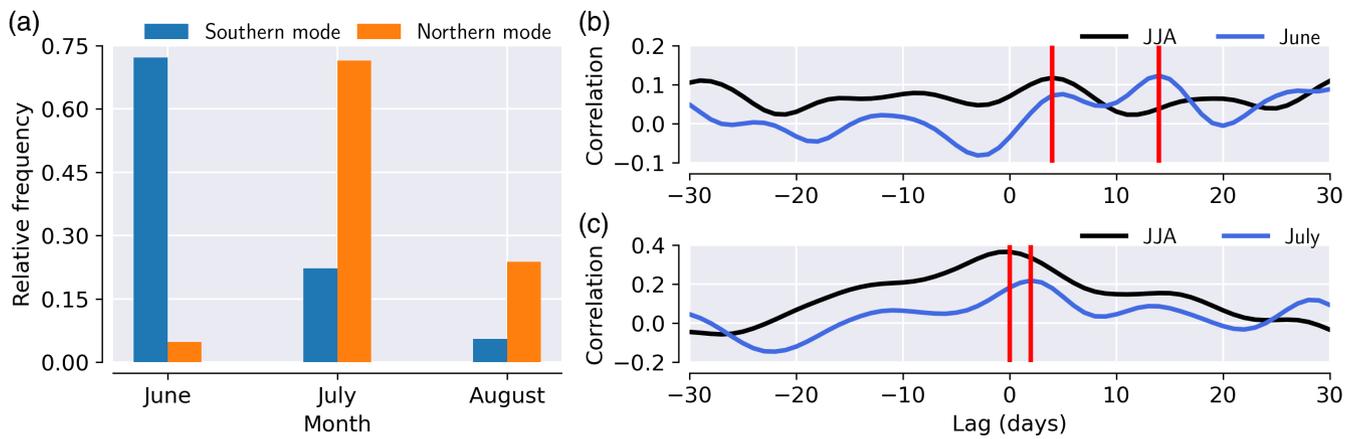
FIGURE 2 (a) The month-wise distribution of days with high ERE synchronization for the southern mode (ARB → SCN) and the northern mode (CMZ → NCN). Lead–lag correlations of low-pass filtered time series of spatially averaged daily numbers of extreme rainfall events (>90th percentile) in ARB and SCN (b, southern mode) and CMZ and NCN (c, northern mode) [Colour figure can be viewed at wileyonlinelibrary.com]
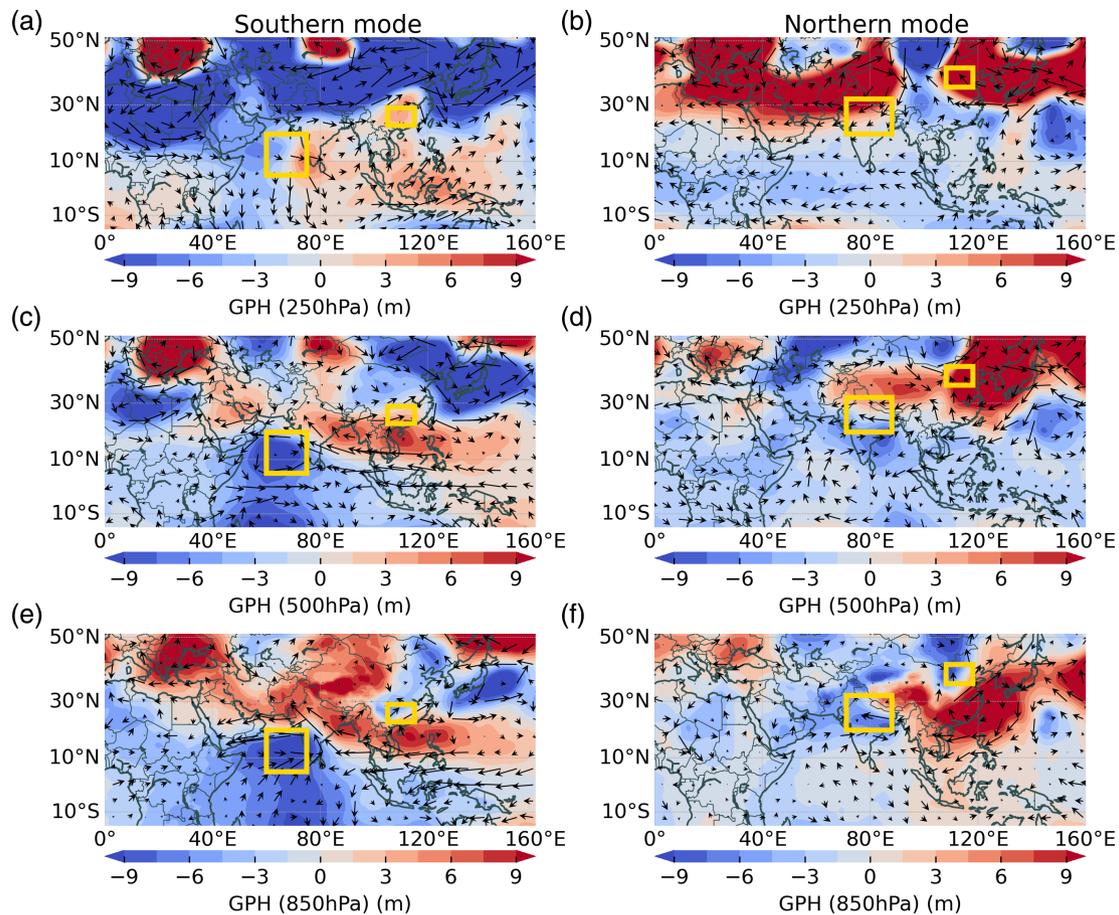
FIGURE 3 Composite anomalies of geopotential height at 250, 500 and 850 hPa, with respect to JJA climatology, based on the days of high ERE synchronization on Day 0, for southern (a, c, e) and northern (b, d, f) modes of ISM–EASM connection [Colour figure can be viewed at wileyonlinelibrary.com]

the horizontal wind field at different pressure levels (see section 2.1), based on the days of strong synchronization (Day 0) for both modes of the ISM–EASM connection (see section 2.3.4). The anomalies are calculated with respect to the JJA seasonal climatology.
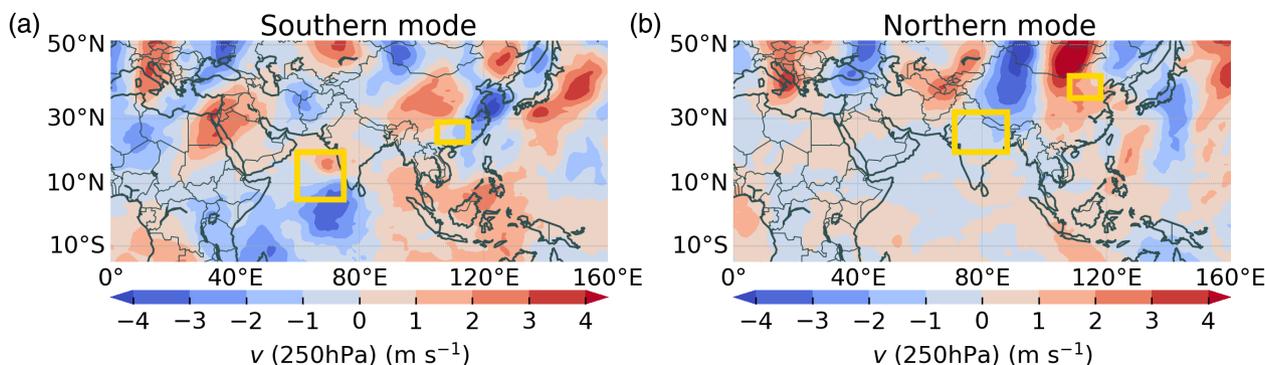
FIGURE 4 Composite anomalies of upper-level meridional wind component v at 250 hPa, with respect to JJA climatology, based on the days of high ERE synchronization on Day 0, for the southern (a) and northern (b) modes of the ISM–EASM connection [Colour figure can be viewed at wileyonlinelibrary.com]

3.3.1 | Southern mode

Geopotential height and wind

Figure 3 provides the composite anomalies of the geopotential height (GPH) and wind field at 250, 500 and 850 hPa, respectively, on Day 0 for the southern mode of the connection. We also show the corresponding composite anomalies of the wind direction field during those times on the GPH-plots. In the upper-level of the troposphere (250 hPa) (Figure 3a), we find an anomalous high-pressure system over the tropics, spanning over the Indian Ocean up to South Asia—covering the Indian subcontinent, the Mainland Southeast Asia up to the Yangtze basin and the Maritime continent. A deep low-pressure zone is present over the rest of the continent. There is also a strengthened upper-westerly jet stream flowing further north of the high GPH region. Strong westerly winds mark the northern boundary of the high GPH region, north of the Yangtze basin, as also seen from the upper-level meridional (v) wind component in Figure 4a. The position of the anomalous high GPH in the upper troposphere controls both the ISM and the rainfall over SCN, which explains the relationship between ARB and SCN. The wave pattern seen in the upper-level meridional wind composite anomalies (Figure 4a) originates from North Africa to East Asia along the mid-latitude westerly jet (Lu et al., 2002). The wavenumbers $k = 7$, 11 are associated with this pattern, as determined from the spatial power spectral density of the latitude belt from 25°N to 35°N (see Figure S5a). The westerly zonal flow is anomalously strong, which may explain the high correlation between rainfall in ARB and SCN at a lag of 4 days during JJA (see Figure 2b).

In the mid-level (500 hPa; see Figure 3c) and lower-level atmosphere (850 hPa; Figure 3e), there is a cyclone formation over the ARB, and also an enhanced western North Pacific subtropical high (WNPSH) south of 20°N and extending to the Bay of Bengal, whose position determines the region of convergence of winds. At low levels we see a cross-equatorial southwesterly wind coming from Somalia hitting the southwestern coast of India. The wind direction in the southern part of the WNPSH over the Bay of Bengal is easterly. This easterly wind meets the above mentioned westerly wind flow at the Malabar coast leading to the ISM onset (Liu and Ding, 2008a; Lee et al., 2013b; Liu et al., 2019). As the location of both the cyclone and the western margin of WNPSH moves northeastward over the course of the next few days, the region of convergence shifts from ARB and south India via the Bay of Bengal to the South China Sea to SCN (Lu and Dong, 2001; Lee et al., 2013b). As we will discuss later, the WNPSH shifts over to Japan in about a month as seen from the GPH 500 hPa (Figure 3d) and 850 hPa (Figure 3f) plots of the northern mode, which peaks in July.

Vertically integrated water vapour flux

Although there is a high correlation between ARB and SCN at a lag of 4 days for the entire JJA season (Figure 2b), the aggregates of IVT composite anomalies (Figure 5a) for Days 0–4 still show separate moisture sources for south India and the Yangtze basin. The water vapour transport pattern highlights the Somalian low-level jet and the Zanzibar current along it, as the main sources of moisture to ARB and hence the onset of ISM (Figure 5a) (Pathak et al., 2017). On the other hand, the predominant moisture sources of SCN during this time are the South China Sea and the adjacent gulf regions (Cheng and Lu, 2020).

However, when we compute the aggregates of IVT composite anomalies for Days 0–14 (since the highest correlation is seen at a lag of 14 days between ARB and SCN for June; see Figure 2b), a continuous path of anomalously high moisture transport is established between the two regions via the Bay of Bengal (Figure 5c). Therefore, a convergence of the intense water vapour transport from the
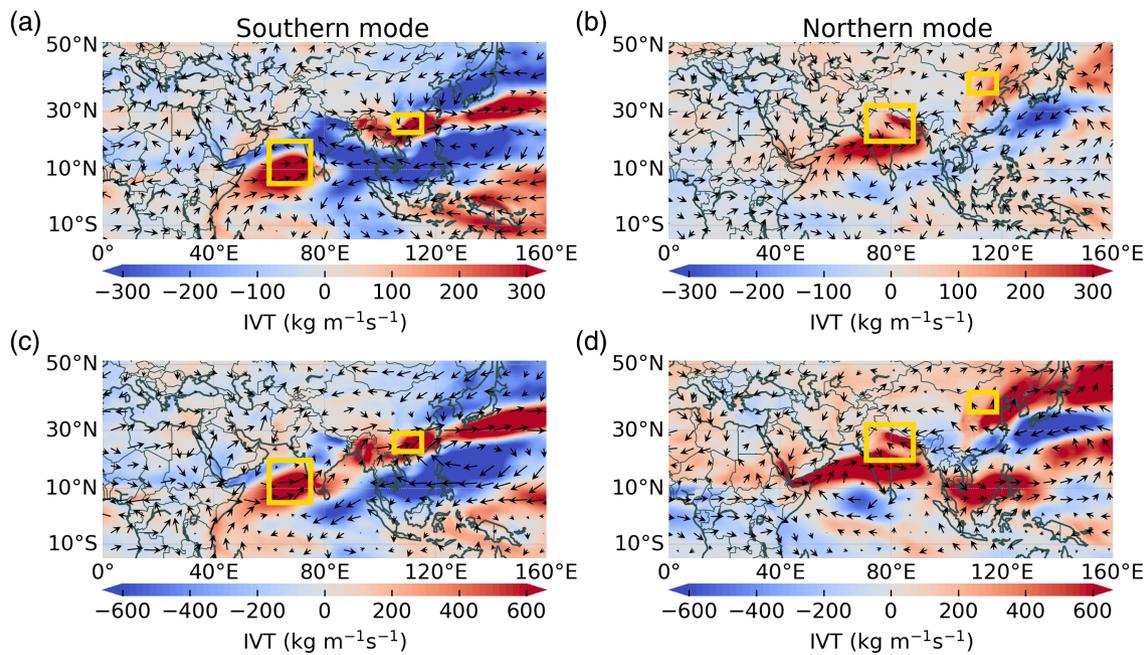
FIGURE 5 Aggregates of composite anomalies of vertically integrated water vapour flux, with respect to JJA climatology, for the southern mode for days (a) 0–4 and (c) 0–14. The same is also shown for the northern mode for days (b) 0–2 and (d) 0–14. Day 0 corresponds to days of high ERE synchronization for each mode of the ISM–EASM connection [Colour figure can be viewed at wileyonlinelibrary.com]

western Indian Ocean and the Pacific Ocean sources occurs in about 2 weeks via the Bay of Bengal, establishing a moisture corridor which coincides with the dominant route of the East Asian atmospheric river (Zhou and Yu, 2005; Yang et al., 2018; Pan and Lu, 2019). The structure and period of formation of the moisture corridor is similar to that of the third stage of the climatological annual cycle of the East Asian atmospheric river catalogued by Pan and Lu (2020), which lasts approximately from 11 June to 1 July. The moisture pathway transports water vapour from the western Indian Ocean to the ARB, India, the Bay of Bengal, and then extends to the north of the Indo-China peninsula, South China Sea, eastern China, and further northeastward to Japan (Figures 5c and S6a). Hence, the establishment of the moisture corridor over the course of 2 weeks between ARB and SCN explains the southern mode of the connection between ISM and EASM. Furthermore, we see from Figure 5a,c that although the heavier rainbelt along the SCN follows from a convergence of southwesterly tropical and mid-latitude northeast moisture sources, the tropical water vapour transport actually originates from the Philippine Sea, as was also noted by Zhou and Yu (2005).
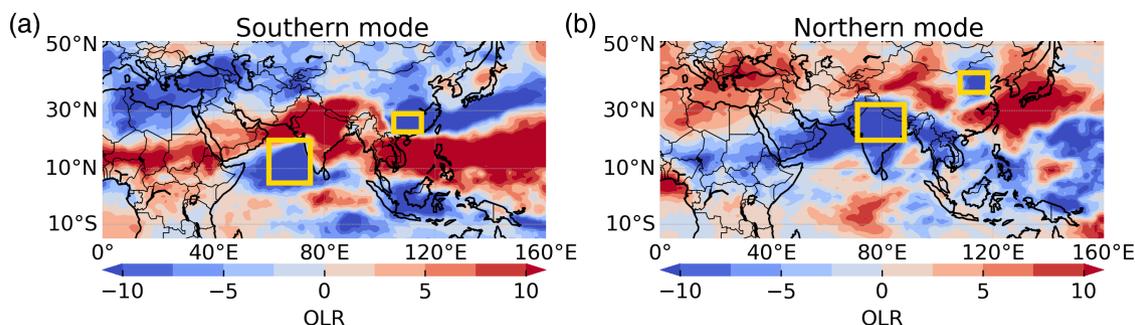
3.3.2 | Northern mode

Geopotential height and wind
In the upper troposphere (250 hPa), we see a strong anomalous high in Figure 3b over Eurasia, roughly north

of 20°N. However, the GPH 250 hPa height is not smooth over the entire continent. In the 250 hPa wind field (Figure 3b), we identify an anticyclone–cyclone–anticyclone (A-C-A) circulation pattern, along a southwestern–northeastern direction (Wei et al., 2014; 2017). There is an anomalous high over west central Asia and parts of the Tibetan Plateau west of 90°E (Wang et al., 2001), and a westerly wind is found north of the Tibetan Plateau. The other subtropical anticyclone is formed over parts of northeast China and predominantly over Japan (Enomoto et al., 2003; Ding and Chan, 2005).

At 500 hPa (Figure 3d), a high in the east and low in the west is seen. The WNPSH is further up in the northeast with a protruding tilt in towards the southwestward direction. There is a sustained low over the Indian subcontinent (Krishnamurthy and Ajayamohan, 2010; Hunt and Fletcher, 2019) with a formation of a deep trough over Kazakhstan. In the lower level (Figure 3f), we observe a deepened low-pressure trough over India, a higher ridge over the eastern Tibetan Plateau and a low over NCN. The enhanced WNPSH is now further northeast as in GPH 500 hPa with a protruding part over Japan as is also seen for the mid-level. The above circulation features are known to be related to strong ISM (Straus and Krishnamurthy, 2007) and are also favourable conditions for causing abundant rainfall over NCN (Lau and Li, 1984; Nitta and Hu, 1996; Chang et al., 2000; Ding and Chan, 2005).

The composite anomalies of the upper-level meridional wind component *v* (Figure 4b) show a

FIGURE 6 Composite anomalies of outgoing long-wave radiation, with respect to JJA climatology, based on the days of high synchronization on Day 0, for (a) southern and (b) northern modes of ISM–EASM connection [Colour figure can be viewed at wileyonlinelibrary.com]

large-scale wave train stretching across Eurasia. The dominant wavenumbers associated with this wave pattern (Figure 4b), $k = 5, 8$, are lower than those for the southern mode, as determined from the spatial power spectral density of the latitude belt from 40°N to 50°N (see Figure S5b). This denotes the propagation of quasi-stationary Rossby wave energy along the east Asian jet, also named as the "Silk Road teleconnection pattern" (Enomoto et al., 2003; Kosaka et al., 2009). The Eurasian wave train, originating in the jet exit region of the North Atlantic, may be affecting the west central Asian high and, thus, the intensity of the ISM (Ding and Wang, 2005). The upper-level anticyclone over west central Asia results in an enhanced convection over India, inducing rainfall (Yanai and Wu, 2006; Ding, 2007). The anticyclone is perturbed by the stationary waves along the Asian jet in late July (Enomoto, 2004). The propagation of the quasi-stationary Rossby waves downstream along the jet and their accumulation in the jet-exit region near Japan forms the anticyclone over Japan (Enomoto et al., 2003). In the meantime, the WNPSH moves northward in the lower and mid troposphere as Meiyu/Baiu fades away. This forms a deep barotropic ridge throughout the troposphere over Japan with a slight westward tilt called the Bonin high (Enomoto et al., 2003; Enomoto, 2004), as seen from the GPH plots (Figure 3b,d,f). However, the deepened low over NCN in the lower-troposphere in contrast to the high in Japan indicates enhanced convection over NCN, inducing increased rainfall, while Japan experiences dry spells during this period. Ambrizzi et al. (1995) through an upper-tropospheric streamfunction teleconnectivity map and time-lag cross-correlation analysis showed that the wave pattern emanates downstream eastward to the Pacific from the base point (35°N, 75°E), in about 3 days (see Ambrizzi et al., 1995, fig. 7). Therefore, the propagation of the quasi-stationary Rossby wave establishes the connection between the strong ISM rainfall over CMZ and the

concurrent extreme rainfall over NCN (Kripalani and Kulkarni, 2001; Ding, 2007). The amplification of the same Rossby wave train upstream due to strengthening of the upper-level anticyclone over west central Asia was also identified as the plausible reason behind the connection of extreme rainfall between Europe and ISM by Boers et al. (2019), who noted that the specific times for Europe–ISM rainfall synchronization are more in July and August than in June and September.

Vertically integrated water vapour flux
We find that although there might be a slight lag of about 1–2 days in the occurrence of rainfall at NCN with respect to the CMZ (Figure 2c), there is mostly a local recycling of moisture from the Pacific Ocean and Indian Ocean sources, respectively, as seen from the aggregate of IVT composite anomalies, not only for Days 0–2 (Figure 5b) but also for Days 0–14 (Figure 5d). Unlike most previous studies (Liu and Ding, 2008b; Liu et al., 2019), which identify the southwesterly moisture flow in the monthly IVT composites as the cause of the connection between rainfall over India and northern China, we uncover from the composites of IVT anomalies for days of high synchronization that sufficient moisture is not transported directly via a tropospheric path. As expected, the above inference is not clearly evident from the IVT composites of Day 0 (see Figure S6b), where the general direction of flow is still southwesterly. Dethof et al. (1999) observed moistening of the lower stratosphere in the Asian monsoon region and suggested a northward moisture transport towards the Pacific from the monsoon anticyclone in July along the upper tropospheric jet stream.

From the above observations of the composite anomalies of atmospheric variables, it is highly likely that the quasi-stationary Rossby waves are the common driver of extreme precipitation in CMZ and NCN, affecting the intensity of rainfall in both regions.
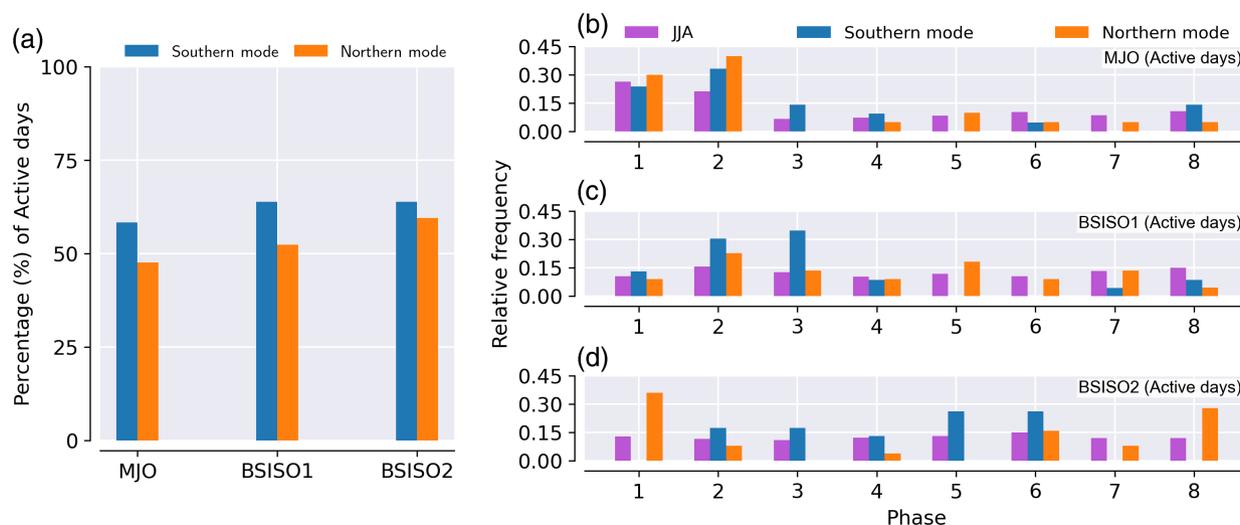
FIGURE 7 (a) Percentage of active (amplitude >1) MJO, BSISO1 and BSISO2 days among the specific days of high ERE synchronization for the southern and northern modes. MJO/BSISO phase distribution for days during the JJA season (for reference) and days of ERE synchronization for southern and northern modes which had *active* MJO (b), BSISO1 (c) and BSISO2 (d) [Colour figure can be viewed at wileyonlinelibrary.com]

3.4 | Role of intraseasonal oscillations

Tropical intraseasonal oscillations (ISOs) are an important source of variability of the Asian Summer Monsoon at short time scales (Serra *et al.*, 2014). They are mainly given by two modes: the Madden–Julian oscillations (MJO) and the boreal summer ISO (BSISO). The MJO, eastward propagating along the equatorial region, in spite of having a weaker variability during boreal summers as compared to that in the boreal winter (Madden and Julian, 1994; Wheeler and Hendon, 2004; Zhang, 2005), has a considerable influence on the variability of the monsoon at intraseasonal timescales (Pai *et al.*, 2011; Bhatla *et al.*, 2017; Li *et al.*, 2019). However, BSISO (Wang and Xie, 1997; Lee *et al.*, 2013a; Chen and Wang, 2021), which has a prominent northward propagation and extends further northward from the equator, is the prevalent ISO mode responsible for the short-term climate variability of the monsoon (Yasunari, 1979; Murakami, 1983; Wang *et al.*, 2005; Yun *et al.*, 2008; Kulkarni *et al.*, 2011; Li *et al.*, 2015; Xia *et al.*, 2021). While the MJO has a periodicity of 30–60 days, the BSISO exhibits two different periodicities: BSISO1 with a periodic cycle of 30–60 days and BSISO2 recurring every 10–20 days. Several works have previously investigated the influence of the ISO on the onset of the ISM and EASM (Wang and Xie, 1997; Kang *et al.*, 1999; Lee *et al.*, 2013a), the active/ break phases of the monsoon (Annamalai and Slingo, 2001; Ding, 2009; Lau and Waliser, 2011; Di Capua *et al.*, 2020) and seasonal mean rainfall (Goswami and Mohan, 2001; Krishnamurthy and Shukla, 2007; Krishnamurthy, 2008) of the ISM and EASM separately.

However, less attention has been paid to its possible role in establishing a connection between the ISM and EASM. Many previous works have suggested that the ISO can not only be a possible triggering mechanism for the sudden onset of monsoon, but can also play a crucial role in the northward progression of the EASM (Qian *et al.*, 2002; Ding and Chan, 2005). This poses an important question about the possible role of ISO in the shifting of synchronization between the ISM and the EASM from the southern to the northern mode. In the following, we investigate the impact of the MJO and BSISO on each of the two discovered modes of ISM–EASM connection by classifying the days of high rainfall synchronization between both pairs of regions (ARB-SCN and CMZ-NCN) into active (amplitude >1) and inactive MJO/BSISO days, and by classifying the active days according to the different BSISO/MJO phases (see section 2.1).

Figure 6 shows the outgoing long-wave radiation (OLR) composite anomalies of both the southern and the northern mode of the ISM–EASM connection. The presence of a negative OLR anomaly, that is, enhanced convective activity, simultaneously in both ARB and SCN (CMZ and NCN) indicates the synchronization in rainfall in case of the southern (northern) connection mode. From Figure 7a, we see that ~40% of the days of high rainfall synchronization are inactive in BSISO/MJO. This suggests that ISO is not the sole factor causing the two modes of ISM–EASM connection. This can also be inferred from the OLR composite anomalies of inactive BSISO/MJO days of high rainfall synchronization, which show simultaneous negative OLR anomaly in the pair of regions for each mode (see Figure S7) aside from similar

TABLE 1 Summary of ISM–EASM connection

Feature		Southern mode	Northern mode
Synchronization pathway		Arabian Sea and southwest coast of India (ARB) with parts of southeastern China (SCN; near the middle and lower reaches of Yangtze River)	Core monsoon zone of India (CMZ; central and northern parts) with northern China (NCN; near the Yellow River valley)
Time of high synchronization		June	July
Anomalous atmospheric circulation	250 hPa	Anomalous high over upper Indian Ocean, peninsular India and Maritime continent; strong westerly jet stream current north of high GPH region in the mid-latitudes; wave train originating from North Africa along the westerly jet	Undulating anomalously high GPH over Eurasia with anticyclone (Tibetan Plateau)–cyclone–anticyclone (central China) pattern; Eurasian wave-train, originating in the jet-exit region of the North Atlantic—dominant Silk Road teleconnection
	500 hPa	Western North Pacific subtropical high (WNPSH) stretching up to Bay of Bengal. Convergence of southwesterly winds from Somalian Coast with easterly winds in the southern edge of the WNPSH over the southwest coast of India	WNPSH further northwest over Pacific and Japan with a southwest protruding tilt, sustained low over Indian subcontinent
	850 hPa	Same as 500 hPa	Indian low, high over eastern Tibetan Plateau and low over NCN
Anomalous vertically integrated water vapour transport		Establishment of moisture corridor in about 2 weeks, transporting moisture from ARB to SCN via the Bay of Bengal and South China Sea	Mostly local circulation of moisture–CMZ from Indian Ocean sources and NCN from Pacific Ocean sources
Intraseasonal oscillation	MJO	Phases 1 and 2	Phases 1 and 2
	BSISO1	Phases 2 and 3	Phases 2 and 5
	BSISO2	Phases 2–6	Phases 6–1

observations made from the OLR composite anomalies of active days (see Figure S8).

Next, we classify the MJO/BSISO active days of high ERE synchronization (Figure 7b–d) on the basis of their different phases. We see that particular phases are associated with enhanced rainfall synchronization between ISM and EASM. MJO Phases 1 and 2 favour synchronization for both northern and southern modes (Figure 7b). Similar observations were made by Boers et al. (2019) in case of link bundles connecting ISM with regions of East Asia and the northwest Pacific Ocean. In case of BSISO1, which has a similar periodicity as the MJO and is significantly correlated with it, we observe that there is a higher occurrence of extreme rainfall synchronization in Phases 2 and 3 for the southern mode, and in Phase 2 for the northern mode (see Figure 7c). However, it is interesting to note that in case of BSISO2, which has a higher variability, an opposite polarity in the phase distribution is seen (Figure 7d). There is a relatively higher frequency of synchronized days for Phases 2–6 in case of the southern mode. On the other hand, synchronization is enhanced during Phases 6–1 for the northern mode. This suggests that while particular phases of the MJO/BSISO1 lead to

an overall increase in the extreme rainfall synchronicity between ISM and EASM, BSISO2 possibly supports the shifting between the modes. The main features of the ISM–EASM connection are summarized in Table 1.

4 | CONCLUSION

We have analysed the spatial patterns of extreme rainfall synchronicity of the Asian monsoon region with a particular focus on the relationship between the Indian and the East Asian summer monsoon and its intraseasonal variability. Firstly, we have constructed complex networks of extreme rainfall events using Event Synchronization for the June–July–August season. Using the network degree field, that is, the number of network links attached to each location, we then identified two distinct synchronization modes between the two monsoon systems along with the specific times when each synchronization pathway becomes dominant. This allows us to distinguish between the specific large-scale atmospheric circulation patterns related to each mode (Table 1):

- Southern mode: The synchronization pathway between the Arabian Sea and southeastern China (middle and lower reaches of the Yangtze River valley) is dominant in June. The associated atmospheric circulation patterns are those which lead to the onset of summer monsoon over India. A moisture corridor between the west Indian Ocean sources (Somalian jet and the Zanzibar current) and the western Pacific sources (South China Sea) is established via the Bay of Bengal in about 2 weeks from the Indian monsoon onset, leading to the onset of Meiyu.

- Northern mode: As the Indian summer monsoon progresses inland in July, the path of extreme rainfall synchronization shifts northward, between the core monsoon zone of India and northern China (near the Yellow River valley). While there is no substantial transport of anomalous moisture directly via a moisture pathway, the strengthening of the upper-level wave train due to stationary Rossby waves (the Silk Road teleconnection; Enomoto *et al.*, 2003; Kosaka *et al.*, 2009) leads to synchronous extreme rainfall conditions over both regions.

We have investigated the role of the tropical intraseasonal oscillation in modulating extreme monsoon precipitation over India and East Asia, and in the mutual interaction between the two monsoon systems using the phase distribution of the days of high rainfall synchronization. Through our analysis, we have shown that extreme rainfall events over the Asian monsoon region are favoured by certain phases of the lower frequency mode (MJO, BSISO1), while the higher-frequency mode (BSISO2) may support the switch between the two connection modes. However, more detailed investigation is needed to gain a deeper understanding of the extent of the role played by the intraseasonal oscillation in the synchronization between the Indian and the East Asian summer monsoon.

Our study has provided valuable insights into the complex relationship between the Indian and East Asian components of the Asian summer monsoon system. Such a detailed understanding of the underlying mechanisms of the ISM–EASM interconnection is crucial to improve the subseasonal forecasting of extreme precipitation events. Further extension of this approach, for example, to shed new light on the relation between the Indian monsoon and rainfall associated with the Baiu season over Japan, understanding the role of Rossby waves as a common driver for extreme rainfall over India and East Asia, as well as the construction of prediction schemes using the above findings can be outlined as promising future lines of research.

CONFLICT OF INTEREST
The authors declare no potential conflict of interest.

ORCID
Shraddha Gupta https://orcid.org/0000-0003-4158-9870
Zhen Su https://orcid.org/0000-0002-1585-8187
Niklas Boers https://orcid.org/0000-0002-1239-9034
Jürgen Kurths https://orcid.org/0000-0002-5926-4276
Norbert Marwan https://orcid.org/0000-0003-1437-7039
Florian Pappenberger https://orcid.org/0000-0003-1766-2898

REFERENCES
Ambrizzi, T., Hoskins, B.J. and Hsu, H. (1995) Rossby wave propagation and teleconnection patterns in the austral winter. *Journal of Atmospheric Sciences*, 52, 3661–3672.

Annamalai, H. and Slingo, J. (2001) Active/break cycles: diagnosis of the intraseasonal variability of the Asian summer monsoon. *Climate Dynamics*, 18, 85–102.

Beverley, J.D., Woolnough, S.J., Baker, L.H., Johnson, S.J., Weisheimer, A. and O'Reilly, C.H. (2021) Dynamical mechanisms linking Indian monsoon precipitation and the circumglobal teleconnection. *Climate Dynamics*, 57, 2615–2636.

Bhatla, R., Singh, M. and Pattanaik, D. (2017) Impact of Madden–Julian oscillation on onset of summer monsoon over India. *Theoretical and Applied Climatology*, 128, 381–391.

Boers, N., Bookhagen, B., Marwan, N., Kurths, J. and Marengo, J. (2013) Complex networks identify spatial patterns of extreme rainfall events of the South American monsoon system. *Geophysical Research Letters*, 40, 4386–4392.

Boers, N., Goswami, B., Rheinwalt, A., Bookhagen, B., Hoskins, B. and Kurths, J. (2019) Complex networks reveal global pattern of extreme-rainfall teleconnections. *Nature*, 566, 373–377.

Boers, N., Rheinwalt, A., Bookhagen, B., Barbosa, H.M., Marwan, N., Marengo, J. and Kurths, J. (2014) The South American rainfall dipole: a complex network analysis of extreme events. *Geophysical Research Letters*, 41, 7397–7405.

Chang, C., Zhang, Y. and Li, T. (2000) Interannual and interdecadal variations of the East Asian summer monsoon and tropical Pacific SSTs. Part I: roles of the subtropical ridge. *Journal of Climate*, 13, 4310–4325.

Chen, G. and Wang, B. (2021) Diversity of the boreal summer intraseasonal oscillation. *Journal of Geophysical Research: Atmospheres*, 126, e2020JD034137.

Cheng, T.F. and Lu, M. (2020) Moisture source–receptor network of the East Asian summer monsoon land regions and the associated atmospheric steerings. *Journal of Climate*, 33, 9213–9231.

Choi, K.-S., Wu, C.-C. and Cha, E.-J. (2010) Change of tropical cyclone activity by Pacific–Japan teleconnection pattern in the western North Pacific. *Journal of Geophysical Research: Atmospheres*, 115, D19114.

Dethof, A., O'Neill, A., Slingo, J. and Smit, H. (1999) A mechanism for moistening the lower stratosphere involving the Asian summer monsoon. *Quarterly Journal of the Royal Meteorological Society*, 125, 1079–1106.

Di Capua, G., Kretschmer, M., Donner, R.V., Van Den Hurk, B., Vellore, R., Krishnan, R. and Coumou, D. (2020) Tropical and mid-latitude teleconnections interacting with the Indian summer monsoon rainfall: a theory-guided causal effect network approach. *Earth System Dynamics*, 11, 17–34.

Ding, Q. (2007) Intraseasonal teleconnection between the summer Eurasian wave train and the Indian monsoon. *Journal of Climate*, 20, 3751–3767.

Ding, Q. (2009) Predicting extreme phases of the Indian summer monsoon. *Journal of Climate*, 22, 346–363.

Ding, Q. and Wang, B. (2005) Circumglobal teleconnection in the Northern Hemisphere summer. *Journal of Climate*, 18, 3483–3505.

Ding, Y. (1994) *Monsoons over China*, Atmospheric and Oceanographic Science Library Vol. 16, Dordrecht: Springer.

Ding, Y. and Chan, J. (2005) The East Asian summer monsoon: an overview. *Meteorology and Atmospheric Physics*, 89, 117–142.

Ding, Y., Liang, P., Liu, Y. and Zhang, Y. (2020) Multiscale variability of Meiyu and its prediction: a new review. *Journal of Geophysical Research: Atmospheres*, 125, e2019JD031496.

Enomoto, T. (2004) Interannual variability of the Bonin high associated with the propagation of Rossby waves along the Asian jet. *Journal of the Meteorological Society of Japan. Ser. II*, 82, 1019–1034.

Enomoto, T., Hoskins, B.J. and Matsuda, Y. (2003) The formation mechanism of the Bonin high in August. *Quarterly Journal of the Royal Meteorological Society*, 129, 157–178.

Feldhoff, J.H., Donner, R.V., Donges, J.F., Marwan, N. and Kurths, J. (2012) Geometric detection of coupling directions by means of inter-system recurrence networks. *Physics Letters A*, 376, 3504–3513.

Gadgil, S. and Joseph, P. (2003) On breaks of the Indian monsoon. *Journal of Earth System Science*, 112, 529–558.

Goswami, B.N. and Mohan, R.A. (2001) Intraseasonal oscillations and interannual variability of the Indian summer monsoon. *Journal of Climate*, 14, 1180–1198.

Hersbach, H., Bell, B., Berrisford, P., Hirahara, S., Horányi, A., Muñoz-Sabater, J., Nicolas, J., Peubey, C., Radu, R., Schepers, D., Simmons, A., Soci, C., Abdalla, S., Abellan, X., Balsamo, G., Bechtold, P., Biavati, G., Bidlot, J., Bonavita, M., Chiara, G., Dahlgren, P., Dee, D., Diamantakis, M., Dragani, R., Flemming, J., Forbes, R., Fuentes, M., Geer, A., Haimberger, L., Healy, S., Hogan, R.J., Hólm, E., Janisková, M., Keeley, S., Laloyaux, P., Lopez, P., Lupu, C., Radnoti, G., Rosnay, P., Rozum, I., Vamborg, F., Villaume, S. and Thépaut, J.N. (2020) The ERA5 global reanalysis. *Quarterly Journal of the Royal Meteorological Society*, 146, 1999–2049.

Huffman, G.J., Bolvin, D.T., Nelkin, E.J., Wolff, D.B., Adler, R.F., Gu, G., Hong, Y., Bowman, K.P. and Stocker, E.F. (2007) The TRMM multisatellite precipitation analysis (TMPA): quasi-global, multiyear, combined-sensor precipitation estimates at fine scales. *Journal of Hydrometeorology*, 8, 38–55.

Hunt, K.M. and Fletcher, J.K. (2019) The relationship between Indian monsoon rainfall and low-pressure systems. *Climate Dynamics*, 53, 1859–1871.

Kang, I.-S., Ho, C.-H., Lim, Y.-K. and Lau, K. (1999) Principal modes of climatological seasonal and intraseasonal variations of the Asian summer monsoon. *Monthly Weather Review*, 127, 322–340.

Kosaka, Y., Nakamura, H., Watanabe, M. and Kimoto, M. (2009) Analysis on the dynamics of a wave-like teleconnection pattern along the summertime Asian jet based on a reanalysis dataset and climate model simulations. *Journal of the Meteorological Society of Japan. Ser. II*, 87, 561–580.

Kripalani, R.H. and Kulkarni, A. (2001) Monsoon rainfall variations and teleconnections over South and East Asia. *International Journal of Climatology*, 21, 603–616.

Kripalani, R.H. and Singh, S. (1993) Large scale aspects of India-China summer monsoon rainfall. *Advances in Atmospheric Sciences*, 10, 71–84.

Krishnamurthy, V. (2008) Seasonal persistence and propagation of intraseasonal patterns over the Indian monsoon region. *Climate Dynamics*, 30, 353–369.

Krishnamurthy, V. and Ajayamohan, R. (2010) Composite structure of monsoon low pressure systems and its relation to Indian rainfall. *Journal of Climate*, 23, 4285–4305.

Krishnamurthy, V. and Shukla, J. (2007) Intraseasonal and seasonally persisting patterns of Indian monsoon rainfall. *Journal of Climate*, 20, 3–20.

Kulkarni, A., Kripalani, R., Sabade, S. and Rajeevan, M. (2011) Role of intra-seasonal oscillations in modulating Indian summer monsoon rainfall. *Climate Dynamics*, 36, 1005–1021.

Lau, K.-M. and Li, M.-T. (1984) The monsoon of East Asia and its global associations—a survey. *Bulletin of the American Meteorological Society*, 65, 114–125.

Lau, W.K.-M. and Waliser, D.E. (2011) *Intraseasonal Variability in the Atmosphere-Ocean Climate System*. Berlin, HD: Springer.

Lee, J.-Y., Wang, B., Wheeler, M.C., Fu, X., Waliser, D.E. and Kang, I.-S. (2013a) Real-time multivariate indices for the boreal summer intraseasonal oscillation over the Asian summer monsoon region. *Climate Dynamics*, 40, 493–509.

Lee, S.-S., Seo, Y.-W., Ha, K.-J. and Jhun, J.-G. (2013b) Impact of the western North Pacific subtropical high on the East Asian monsoon precipitation and the Indian Ocean precipitation in the boreal summertime. *Asia-Pacific Journal of Atmospheric Sciences*, 49, 171–182.

Li, J., Mao, J. and Wu, G. (2015) A case study of the impact of boreal summer intraseasonal oscillations on Yangtze rainfall. *Climate Dynamics*, 44, 2683–2702.

Li, X., Gollan, G., Greatbatch, R.J. and Lu, R. (2019) Impact of the MJO on the interannual variation of the Pacific–Japan mode of the East Asian summer monsoon. *Climate Dynamics*, 52, 3489–3501.

Libertino, A., Sharma, A., Lakshmi, V. and Claps, P. (2016) A global assessment of the timing of extreme rainfall from TRMM and GPM for improving hydrologic design. *Environmental Research Letters*, 11, 054003.

Liu, Y. and Ding, Y. (2008a) Teleconnection between the Indian summer monsoon onset and the Meiyu over the Yangtze River valley. *Science in China Series D: Earth Sciences*, 51, 1021–1035.

Liu, Y. and Ding, Y. (2008b) Analysis and numerical simulations of the teleconnection between Indian summer monsoon and precipitation in north China. *Journal of Meteorological Research*, 22, 489–501.

Liu, Y., Liang, P. and Sun, Y. (2019) *The Asian Summer Monsoon: Characteristics, Variability, Teleconnections and Projection*. Amsterdam: Elsevier.

Lu, R. and Dong, B. (2001) Westward extension of North Pacific subtropical high in summer. *Journal of the Meteorological Society of Japan. Ser. II*, 79, 1229–1241.

Lu, R.-Y., Oh, J.-H. and Kim, B.-J. (2002) A teleconnection pattern in upper-level meridional wind over the North African and Eurasian continent in summer. *Tellus A: Dynamic Meteorology and Oceanography*, 54, 44–55.

Madden, R.A. and Julian, P.R. (1994) Observations of the 40–50-day tropical oscillation—a review. *Monthly Weather Review*, 122, 814–837.

Malik, N., Bookhagen, B., Marwan, N. and Kurths, J. (2012) Analysis of spatial and temporal extreme monsoonal rainfall over South Asia using complex networks. *Climate Dynamics*, 39, 971–987.

Marwan, N. and Kurths, J. (2015) Complex network based techniques to identify extreme events and (sudden) transitions in spatio-temporal systems. *Journal of Nonlinear Science*, 25, 097609.

Murakami, M. (1983) Analysis of the deep convective activity over the western Pacific and Southeast Asia part I: diurnal variation. *Journal of the Meteorological Society of Japan. Ser. II*, 61, 60–76.

Nitta, T. and Hu, Z.-Z. (1996) Summer climate variability in China and its association with 500 hPa height and tropical convection. *Journal of the Meteorological Society of Japan. Ser. II*, 74, 425–445.

Pai, D., Bhate, J., Sreejith, O. and Hatwar, H. (2011) Impact of MJO on the intraseasonal variation of summer monsoon rainfall over India. *Climate Dynamics*, 36, 41–55.

Pan, M. and Lu, M. (2020) East Asia atmospheric river catalog: annual cycle, transition mechanism, and precipitation. *Geophysical Research Letters*, 47, e2020GL089477.

Pan, M. and Lu, M. (2019) A novel atmospheric river identification algorithm. *Water Resources Research*, 55, 6069–6087.

Pathak, A., Ghosh, S., Martinez, J.A., Dominguez, F. and Kumar, P. (2017) Role of oceanic and land moisture sources and transport in the seasonal and interannual variability of summer monsoon in India. *Journal of Climate*, 30, 1839–1859.

Qian, W., Kang, H.-S. and Lee, D.-K. (2002) Distribution of seasonal rainfall in the East Asian monsoon region. *Theoretical and Applied Climatology*, 73, 151–168.

Quiroga, R.Q., Kreuz, T. and Grassberger, P. (2002) Event synchronization: a simple and fast method to measure synchronicity and time delay patterns. *Physical Review E*, 66, 041904.

Rajeevan, M., Gadgil, S. and Bhate, J. (2010) Active and break spells of the Indian summer monsoon. *Journal of Earth System Science*, 119, 229–247.

Rehfeld, K., Marwan, N., Breitenbach, S.F. and Kurths, J. (2013) LateHolocene Asian summermonsoon dynamics from small but complex networks of paleoclimate data. *Climate Dynamics*, 41, 3–19.

Runge, J., Petoukhov, V., Donges, J.F., Hlinka, J., Jajcay, N., Vejmelka, M., Hartman, D., Marwan, N., Paluš, M. and Kurths, J. (2015) Identifying causal gateways and mediators in complex spatio-temporal systems. *Nature Communications*, 6, 1–10.

Serra, Y.L., Jiang, X., Tian, B., Amador-Astua, J., Maloney, E.D. and Kiladis, G.N. (2014) Tropical intraseasonal modes of the atmosphere. *Annual Review of Environment and Resources*, 39, 189–215.

Stolbova, V., Martin, P., Bookhagen, B., Marwan, N. and Kurths, J. (2014) Topology and seasonal evolution of the network of extreme precipitation over the Indian subcontinent and Sri Lanka. *Nonlinear Processes in Geophysics*, 21, 901–917.

Straus, D.M. and Krishnamurthy, V. (2007) The preferred structure of the interannual Indian monsoon variability. In: *Atmospheric and Oceanic*. Basel: Birkhäuser Basel, pp. 1717–1732.

Wang, B., Webster, P.J. and Teng, H. (2005) Antecedents and self-induction of active-break south Asian monsoon unraveled by satellites. *Geophysical Research Letters*, 32, L04704.

Wang, B., Wu, R. and Lau, K.-M. (2001) Interannual variability of the Asian summer monsoon: contrasts between the Indian and the western North Pacific–East Asian monsoons. *Journal of Climate*, 14, 4073–4090.

Wang, B. and Xie, X. (1997) A model for the boreal summer intraseasonal oscillation. *Journal of the Atmospheric Sciences*, 54, 72–86.

Wei, W., Zhang, R., Wen, M., Rong, X. and Li, T. (2014) Impact of Indian summer monsoon on the South Asian high and its influence on summer rainfall over China. *Climate Dynamics*, 43, 1257–1269.

Wei, W., Zhang, R., Wen, M. and Yang, S. (2017) Relationship between the Asian westerly jet stream and summer rainfall over central Asia and north China: roles of the Indian monsoon and the South Asian high. *Journal of Climate*, 30, 537–552.

Wheeler, M.C. and Hendon, H.H. (2004) An all-season real-time multivariate MJO index: development of an index for monitoring and prediction. *Monthly Weather Review*, 132, 1917–1932.

Wolf, F., Ozturk, U., Cheung, K. and Donner, R.V. (2021) Spatio-temporal patterns of synchronous heavy rainfall events in East Asia during the Baiu season. *Earth System Dynamics*, 12, 295–312.

Woo, S., Singh, G.P., Oh, J.-H. and Lee, K.-M. (2019) Possible tele-connections between East and South Asian summer monsoon precipitation in projected future climate change. *Meteorology and Atmospheric Physics*, 131, 375–387.

Wu, R. (2017) Relationship between Indian and East Asian summer rainfall variations. *Advances in Atmospheric Sciences*, 34, 4–15.

Xia, Y., Huang, Q., Yao, S. and Sun, T. (2021) Multiscale analysis of persistent heavy rainfall in the Meiyu period over the middle and lower reaches of the Yangtze River. *Frontiers in Earth Science*, 9, 668.

Yanai, M. and Wu, G.-X. (2006) *Effects of the Tibetan Plateau*. Berlin-Heidelberg: Springer, pp. 513–549. https://doi.org/10.1007/3-540-37722-0_13.

Yang, Y., Zhao, T., Ni, G. and Sun, T. (2018) Atmospheric rivers over the Bay of Bengal lead to northern Indian extreme rainfall. *International Journal of Climatology*, 38, 1010–1021.

Yasunari, T. (1979) Cloudiness fluctuations associated with the Northern Hemisphere summer monsoon. *Journal of the Meteorological Society of Japan. Ser. II*, 57, 227–242.

Yun, K.-S., Ren, B., Ha, K.-J., Chan, J. and Jhun, J.-G. (2008) The 30–60-day oscillation in the East Asian summer monsoon and its time-dependent association with the ENSO. *Tellus A: Dynamic Meteorology and Oceanography*, 61, 565–578.

Zhang, C. (2005) Madden–Julian oscillation. *Reviews of Geophysics*, 43, RG2003.

Zhou, T.-J. and Yu, R.-C. (2005) Atmospheric water vapor transport associated with typical anomalous summer rainfall patterns in China. *Journal of Geophysical Research: Atmospheres*, 110, D08104.

SUPPORTING INFORMATION

Additional supporting information can be found online in the Supporting Information section at the end of this article.